ROTOR BLADE MODELING IN A HELICOPTER MULTI BODY SIMULATION BASED ON THE FLOATING FRAME OF REFERENCE FORMULATION

Felix Weiss*, Joshua Merlis*, Reinhard Lojewski*, Johannes Hofmann*,
Melven Roehrig-Zoellner[§]

German Aerospace Center (DLR),
*Institute of Flight Systems, Lilienthalplatz 7, 38108 Brunswick, Germany
[§]Institute for Software Technology, Linder Hoehe, 51147 Cologne, Germany

Felix.Weiss@dlr.de

Abstract

The Floating Frame of Reference formulation was chosen to include the *Beam Advanced Model* in DLR's Versatile Aeromechanics Simulation Tool. During the development and concurrent testing of the model in the field of helicopter rotor dynamics, some particular shortcomings have become apparent. These mainly – but not exclusively – concern inertial loads affecting the flexible motion of beams. This paper treats the related physical phenomena, and proposes enhancements to the model which remedy the deficiencies of the baseline method. Particular attention is given to the introduction of rotational shape functions to account e.g. for the propeller moment and the consideration of an accelerated Floating Frame of Reference to address the blade attachment's radial offset from the rotor center in the centrifugal field. Furthermore, the application of external loads (e.g. airloads) away from the beam's nodes or off the beam axis is addressed as a prerequisite for independent structural and aerodynamic discretization. Finally, the modal reduction under centrifugal loading is considered. The individual model upgrades are verified based on analytical reference results of appropriate rotor dynamics test cases. The enhancements are necessary for simulating flexible helicopter rotor blades within a Multi Body System – a feature required for sophisticated simulation scenarios in which the limitations of conventional rotor models (e.g. constant rotational hub speed) are exceeded.

NOTATION

Abbreviations

1D	1-dimensional
3D	3-dimensional
BAM	Beam Advanced Model
DoF	Degrees of Freedom
ERF	Element Reference Frame
FE	Finite Element
FFR	Floating Frame of Reference
F*i*	i^{th} blade flap mode, $i = 1, 2, 3, \ldots$
L*i*	i^{th} blade lead-lag mode, $i = 1, 2, 3, \ldots$
MBS	Multi Body System
ODE	Ordinary Differential Equations
T*i*	i^{th} blade torsion mode, $i = 1, 2, 3, \ldots$
VAST	Versatile Aeromechanics Simulation Tool

Symbols

A	(m^2)	area
a	$(\mathrm{m/s}^2)$	translatory acceleration
$\mathbf{D}_{ff}$	(Nms)	damping matrix of FE system
e	(m)	hinge offset from rotor center
F^c	(N)	centrifugal force
F_e	(N)	external force
g	$(\mathrm{m/s}^2)$	acceleration due to gravity
$\mathbf{I}$	$(-)$	identity matrix
I_{ij}	$(\mathrm{div.})$	cross sectional mass moment of order $ij = 00, 10, 01, 20, 02, 11$ in ξ and η, respectively
$\bar{\mathbf{J}}_{\theta f}$	(kgm^2)	coupling: rigid rot. – flexible
$\bar{\mathbf{J}}_{\theta\theta}$	(kgm^2)	rigid rotational inertia tensor
$\mathbf{J}_{\mathrm{DoF}}$	$(-)$	matrix to remove locked DoF
$\mathbf{K}_{ff}$	(Nm)	stiffness matrix of FE system
$\mathbf{K}^*_{\mathrm{free}}$	(Nm)	extended stiffn. mat. (free DoF)
$\mathbf{M}_{ff}$	(kgm^2)	mass matrix of FE system
M^c	(Nm)	moment due to centrifugal forces
M_e	(Nm)	external moment
M^g	(Nm)	gyroscopic moment
M_p	(Nm)	propeller moment
m	(kg)	mass
$\mathbf{m}_{RR}$	(kg)	rigid translatory mass matrix
n	$(-)$	chosen number of eigenmodes
n_r	$(-)$	number of FE system's DoF
Q	$(\mathrm{div.})$	right hand side load terms
r_{I}	$(-)$	flexible position states
r_{II}	$(1/\mathrm{s})$	flexible velocity states, $r_{\mathrm{II}} = \dot{r}_{\mathrm{I}}$
$\mathbf{S}_{\mathrm{rot}}$	(rad)	rot. shape function matrix
$\mathbf{S}_{\mathrm{tra}}$	(m)	transl. shape function matrix
$\bar{\mathbf{S}}$	(kgm)	coupling: rigid translatory – flex.
$\tilde{\bar{\mathbf{S}}}_t$	(kgm)	coupling: rigid transl. – rigid rot.
$\mathbf{T}$	$(-)$	rot. matrix: FFR to marker frame
$\mathbb{T}$	$(-)$	rot. matrix analogous to $\mathbf{T}$, but for nodal states instead of 3D vector
$\mathbf{T}_{\mathrm{ERF}}$	$(-)$	rotation matrix from FFR to ERF
$\mathbf{T}_{\mathrm{flex}}$	$(-)$	flexible rotation matrix
$\mathbf{T}_{\mathrm{mark}}$	$(-)$	rotation matrix: ERF to marker frame (undeformed)
$\bar{u}$	(m)	location relative to FFR
u_x	(m)	axial elongation
V	(m^3)	volume
v	$(\mathrm{m/s})$	translatory velocity
u_i	$(-)$	FE system's i^{th} eigenvector
x	(m)	axial coordinate
η	(m)	vertical coordinate
ϑ	$(^\circ)$	twist angle
ξ	(m)	lateral coordinate
ρ	$(\mathrm{kg/m}^3)$	mass density
Ω	$(\mathrm{rad/s})$	rotor speed
ω	$(\mathrm{rad/s})$	angular velocity
ω_i	$(\mathrm{rad/s})$	FE system's i^{th} eigenfrequency

Indices, accentuations, and operators

$()_0$	undeformed
$()_{75}$	value at 75% rotor radius
$()^c$	centrifugal
$()_e$	external
$()^f$	flexible motion
$()^g$	gyroscopic
$()_g$	gravity
$()^R$	rigid translatory motion
$()_{\mathrm{flex}}$	due to deformation
$()_{\mathrm{free}}$	reduced to the free DoF
$()_{\mathrm{pre}}$	undeformed (e.g. pre-twist)
$()_{\mathrm{ref}}$	reference or nominal value
$()_{\mathrm{rot}}$	rotational
$()_{\mathrm{tra}}$	translatory
$()_v$	inertial
$()^\theta$	rigid rotational motion
$X^{(\mathrm{frame})}$	quantity X expressed in specified frame (instead of the FFR)
$\mathbf{X}^\top$	transpose of a matrix $\mathbf{X}$
$\dot{X}$	time derivative of X
X'	spatial derivative of X
$\bar{X}$	quantity X relative to the FFR
$\tilde{X}$	cross product operator for vector X

1. INTRODUCTION

The structural modeling and analysis of helicopters with a multitude of flexible components is a demanding task. A rotor blade, for example, is exposed to large centrifugal loads. Furthermore, its rigid flap, lead-lag and torsion motion as well as the associated flexible modes are coupled not only through the acting airloads, but also by kinematic, elastic, and gyroscopic effects. Conventionally, rotor blades are modeled based on the theory of beams rotating at a certain rotor speed with invariant boundary conditions. While these models provide results of sufficient accuracy for many applications, some specific use cases require more sophisticated structural models. These include, for instance, the detailed simulation of the rotor blade attachment containing hinges, rigid connections, flexible elements, springs and dampers as well as the resolution of structural couplings between the arbitrarily moving fuselage, the drivetrain, and the rotor blades. On top of that, arbitrary system configurations such as helicopters, multi-rotor vehicles, and wind turbines require versatile configuration options. An approach to address these issues is the Multi Body System (MBS) model.

In DLR's Versatile Aeromechanics Simulation Tool (VAST)[1], the structural core of the aeromechanic

model is comprised of an MBS. It includes an exact formulation of the non-linear rigid body kinematics. The MBS is implemented in C++ with a class architecture based on structures of arrays to allow "single-instruction-multiple-data" optimizations; it features container classes for bodies, joints and force elements. The MBS formalism is based on a set of minimal states which are comprised of the joint states and the states representing flexible body deformation. This method yields ordinary differential equations (ODE) of motion which are coupled to those of aerodynamics, control, and further models by the VAST solver. The ODE formalism requires the Jacobians of the bodies' velocities v, angular velocities ω, and flexible velocities $r_{||}$ with respect to the minimal states of the whole MBS. These Jacobians are calculated using automatic differentiation in VAST [2]. This not only improves the maintainability of the code, but also substantially simplifies the inclusion of new flexible body models.

1.1. Beam Advanced Model

One such model is the Beam Advanced Model (BAM) [3], which is integrated in VAST's MBS to accurately simulate modern rotor blades with complex properties. The key innovation of this model is the introduction of four additional degrees of freedom (DoF) on top of the standard three translatory and three rotational nodal DoF. These four additional DoF represent the spatial derivatives of the axial elongation and twist with respect to the element's longitudinal axis ($\mathrm{d}u_x/\mathrm{d}x$, $\mathrm{d}\vartheta/\mathrm{d}x$, see Figure 1).

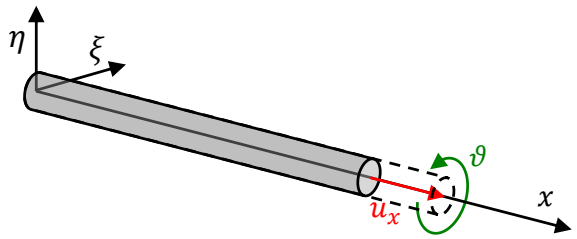

Figure 1: Coordinate directions (x, ξ, η), axial elongation u_x, and flexible twist ϑ

Each of these DoF is computed at the rightmost location of the element to the left of a given node and at the leftmost location of the element to the node's right [3,4]. Considerations of these additional DoF in the finite element formulation enable high-fidelity simulations of abrupt changes in geometrical and physical parameters without the need for fine discretization. BAM therefore offers improved performance for simulating complex beams compared to traditional models. The accuracy of BAM simulations has been demonstrated for modern rotor blade designs, e.g. the Blue Edge™ blade with forward and backward swept portions [3,4].

The original BAM formulation directly handles the effects of centrifugal and gyroscopic loads through additional terms in the element's stiffness and damping matrices [3]. As discussed in the following sections, the present implementation employs BAM in a generalized framework, enabling the consideration of centrifugal and gyroscopic loads with arbitrary motion at the blade connection. To this end, the aforementioned BAM-specific terms were removed from the element matrices and replaced by the generalized terms developed in the following.

1.2. Floating Frame of Reference

BAM has already been integrated in the comprehensive rotor code HOST in a prototypical fashion based on decoupled dynamic equations for the rigid and flexible body motions. [5] For the integration of BAM in the MBS of VAST, in contrast, the well-established Floating Frame of Reference (FFR) formulation [6] has been chosen. In the FFR approach, the elastic position states $r_{|}$ and velocity states $r_{||} = \dot{r}_{|}$ describe the body deformation with respect to the body reference frame. This frame, in turn, is moving arbitrarily ("floating") relative to the inertial frame by v and ω, which are both 3D vectors. They represent the rigid body portion of motion with mass matrix $\mathbf{m}_{RR}$, inertia tensor $\bar{\mathbf{J}}_{\theta\theta}$, and coupling matrix $\tilde{\bar{\mathbf{S}}}_t^{\top}$, see upper part of Equation 1.

The Finite Element (FE) system describes the body's flexible motion and is composed of multiple elements. The second order differential equation of the FE system has been converted to first order form (lower part of Equation 1), in which the mass $\mathbf{M}_{ff}$, stiffness $\mathbf{K}_{ff}$, and damping $\mathbf{D}_{ff}$ matrices are found. $\mathbf{K}_{ff}$ is composed of both the structural stiffness and geometric stiffening terms.

The rightmost entries $\bar{\mathbf{S}}$ and $\bar{\mathbf{J}}_{\theta f}$ in the upper part of Equation 1 constitute coupling terms between the rigid body motion and the flexible motion. The right hand side includes gravity Q_g, inertial loads Q_v, and external loads Q_e acting on the rigid translatory motion (superscript R), the rigid rotational motion (superscript θ) and the flexible motion (superscript f). Note that the loads caused by discrete translatory or rotational springs or dampers, as they are used in rotor models, are part of Q_e.

The FFR-based integration of FE beam models in MBS has already been addressed in the literature, for example in [7]. However, during the implementation and concurrent testing of this formulation using

$$(1)\quad \begin{pmatrix} \mathbf{m}_{RR} & \tilde{\bar{\mathbf{S}}}_t^{\top} & \mathbf{0} & \bar{\mathbf{S}} \\ & \bar{\mathbf{J}}_{\theta\theta} & \mathbf{0} & \bar{\mathbf{J}}_{\theta f} \\ & & \mathbf{I} & \mathbf{0} \\ sym. & & & \mathbf{M}_{ff} \end{pmatrix} \cdot \begin{pmatrix} \dot{v} \\ \dot{\omega} \\ \dot{r}_{|} \\ \dot{r}_{||} \end{pmatrix} = \begin{pmatrix} \mathbf{0} & \mathbf{0} & \mathbf{0} & \mathbf{0} \\ \mathbf{0} & \mathbf{0} & \mathbf{0} & \mathbf{0} \\ \mathbf{0} & \mathbf{0} & \mathbf{0} & \mathbf{I} \\ \mathbf{0} & \mathbf{0} & -\mathbf{K}_{ff} & -\mathbf{D}_{ff} \end{pmatrix} \cdot \begin{pmatrix} v \\ \omega \\ r_{|} \\ r_{||} \end{pmatrix} + \begin{pmatrix} Q_g^R \\ Q_g^{\theta} \\ 0 \\ Q_g^f \end{pmatrix} + \begin{pmatrix} Q_v^R \\ Q_v^{\theta} \\ 0 \\ Q_v^f \end{pmatrix} + \begin{pmatrix} Q_e^R \\ Q_e^{\theta} \\ 0 \\ Q_e^f \end{pmatrix}$$

BAM elements in VAST, some particular issues have become apparent, primarily related to the aforementioned special requirements of helicopter rotor dynamics. These issues mainly – but not exclusively – concern inertial loads Q_v^f acting on flexible motion. The issues and their solutions will be presented in the following.

2. CONFIGURATION

Before treating the details of the FE beam element model, its configuration shall be addressed. To model the dynamic behavior of the beam, its inertial properties – commonly referred to as inertia shape integrals – need to be calculated. As formulated in [6] and [7], inertia shape integrals are integrals over the volume V of the mass density ρ, weighted by different combinations of the 3D location $\bar{u}$ of the volume increment relative to the FFR and the translatory shape function matrix $\mathbf{S}_{\text{tra}} = \mathbf{S}_{\text{tra}}(\bar{u})$ evaluated at this location, for example

$$(2)\quad \bar{\mathbf{J}}_{\theta f} = \int_V \rho \tilde{\bar{u}} \mathbf{S}_{\text{tra}} \, \mathrm{d}V.$$

The tilde symbol denotes the cross product operator according to

$$(3)\quad a \times b = \begin{pmatrix} a_2 b_3 - a_3 b_2 \\ a_3 b_1 - a_1 b_3 \\ a_1 b_2 - a_2 b_1 \end{pmatrix} = \tilde{a} b = \begin{pmatrix} 0 & -a_3 & a_2 \\ a_3 & 0 & -a_1 \\ -a_2 & a_1 & 0 \end{pmatrix} \begin{pmatrix} b_1 \\ b_2 \\ b_3 \end{pmatrix},$$

while the bar (e.g. on $\bar{u}$) indicates that the quantity is given relative to the FFR. Furthermore, if not indicated by a dedicated superscript $X^{(\text{frame})}$, all vectors X are expressed in the coordinates of the FFR. Note that the reference system (relative to what?) and the coordinate system (expressed in which frame?) of a vectorial quantity have to be distinguished.

The BAM configuration does not provide the 3D distribution of ρ, but rather the mass per length $I_{00} = \int_A \rho \, \mathrm{d}A = m'$, as well as the pre-evaluated cross sectional moments $I_{10} = \int_A \rho\xi \, \mathrm{d}A$ and $I_{01} = \int_A \rho\eta \, \mathrm{d}A$, where ξ and η are the local lateral and vertical coordinates, respectively, spanning the cross section A (area with green edge in Figure 2).

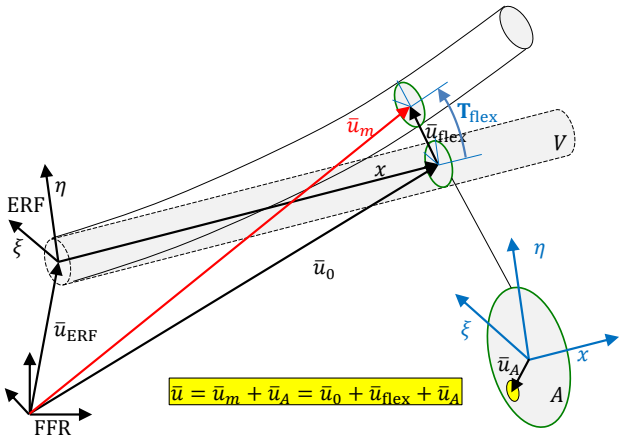

Figure 2: Schematic of 1D integration along the beam axis

The location of the volume increment is depicted as a yellow dot in the zoomed-in cross section view of Figure 2. Its 3D position vector $\bar{u}$ can be split up into that of the cross sectional reference location $\bar{u}_m$, and the location within the cross section $\bar{u}_A$ relative to the reference. $\bar{u}_m$, in turn, has a rigid portion $\bar{u}_0$ and a flexible portion $\bar{u}_{\text{flex}}$. According to $\bar{u} = \bar{u}_m + \bar{u}_A$, the integral can be split up:

$$(4)\quad \bar{\mathbf{J}}_{\theta f} = \int_x \left\{ \int_A \rho \widetilde{(\bar{u}_m + \bar{u}_A)} \, \mathrm{d}A \right\} \mathbf{S}_{\text{tra}} \, \mathrm{d}x = \int_x \tilde{X} \mathbf{S}_{\text{tra}} \, \mathrm{d}x$$

Therein, x denotes the beam element's axial direction. Since $\bar{u}_m$ is constant throughout the cross section, it can be taken outside of the area integral. In the coordinates of the Element Reference Frame (ERF), the vector from the reference location to the volume increment reads $\bar{u}_A^{(\text{ERF})} = (0, \xi, \eta)^{\top}$. Accordingly, the auxiliary cross sectional integral X

can be reformulated:

$$(5)\quad X = \int_A \rho \bar{u}_m \, \mathrm{d}A + \int_A \rho \cdot \mathbf{T}^\top \cdot \bar{u}_A^{(\mathrm{ERF})} \, \mathrm{d}A$$
$$= \bar{u}_m \cdot m' + \mathbf{T}^\top \cdot \begin{pmatrix} 0 \\ I_{10} \\ I_{01} \end{pmatrix}$$

Notes on the coordinate transformation between the ERF and the FFR ($\bar{u}_A = \mathbf{T}^\top \cdot \bar{u}_A^{(\mathrm{ERF})}$) are given in Appendix A.1. The transformations of all other inertia shape integrals from 3D to 1D form are presented in Appendix A.2. The added value is the expression of all inertial properties needed in Equation 1 based on the commonly used cross sectional beam properties m' (0^{th} order mass moment), I_{10}, I_{01} (1^{st} order mass moments), and I_{20}, I_{02} and I_{11} (2^{nd} order mass moments).

3. ROTATIONAL SHAPE FUNCTIONS

According to the theory in [6] and [7], the inertial loads Q_v^f affecting flexible motion read

$$(6)\quad Q_v^f = Q_{v,\mathrm{tra}}^f = -\int_V \rho \mathbf{S}_{\mathrm{tra}}^\top \left(\tilde{\omega}\tilde{\omega}\bar{u} + 2\tilde{\omega}\dot{\bar{u}}\right) \mathrm{d}V.$$

Since $\mathbf{S}_{\mathrm{tra}}$ only includes the three rows for translatory deflections, but not those for rotational deflections, this formulation does not account for the direct effect of inertial loads on the flexible rotation of the beam's nodes. However, in helicopter rotor analysis, there is (at least) one very important effect of inertial loads on flexible rotation: the propeller moment [8,9], which is illustrated in Figure 3. The cross section of a 1D-beam may have different inertial properties in the two cross sectional directions. For example, the lead-lag inertia per unit length of a typical rotor blade cross section is larger than its flap inertia per unit length. In this case, for a rotating blade, the centrifugal forces F^c generate the propeller moment M_p which tends to orient the section flat in the rotor plane of rotation. To model this effect for a 1D-beam, the rotational shape function matrix $\mathbf{S}_{\mathrm{rot}}$ must be taken into account. Analogous to the translatory matrix $\mathbf{S}_{\mathrm{tra}}$, $\mathbf{S}_{\mathrm{rot}}$ has three rows, corresponding to rotations about x, ξ, and η.

The incremental moment $\mathrm{d}M^c$ about the beam axis x, caused by the centrifugal force acting on a mass increment $\mathrm{d}m$, is

$$(7)\quad \mathrm{d}M^c = -\bar{u}_A \times (\omega \times (\omega \times \bar{u}))\, \mathrm{d}m.$$

The effect on flexible rotation results from multiplication with the rotational shape function matrix. Using $\mathrm{d}m = \rho \, \mathrm{d}V$, the additional inertial loads term

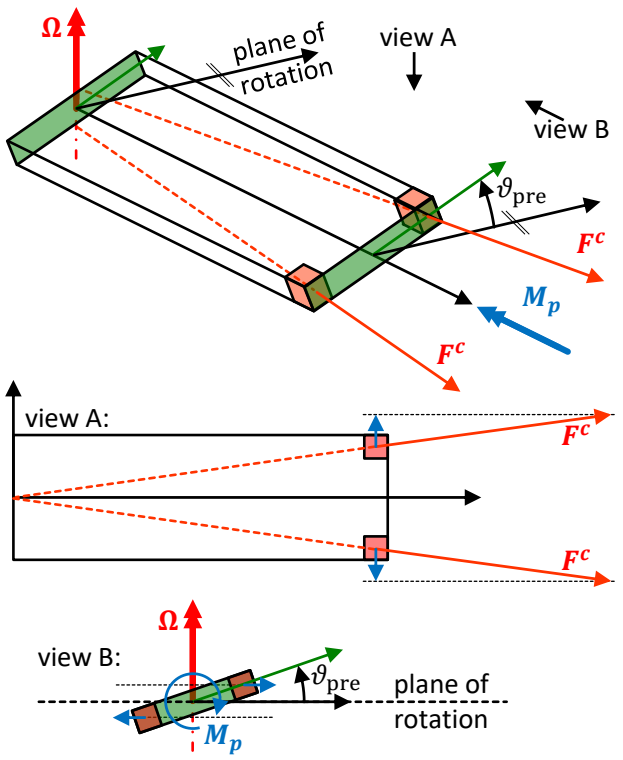

Figure 3: Propeller moment M_p due to pre-twist ϑ_{pre}; *no deformation* shown, i.e. $\vartheta_{\mathrm{flex}} = 0\,^\circ$

affecting flexible motion in integral form is

$$(8)\quad Q_{v,\mathrm{rot}}^{f,c} = -\int_V \rho \mathbf{S}_{\mathrm{rot}}^\top \cdot \bar{u}_A \times (\omega \times (\omega \times \bar{u}))\, \mathrm{d}V.$$

Analogously, the gyroscopic moments

$$(9)\quad \mathrm{d}M^g = -2\,\bar{u}_A \times (\omega \times \dot{\bar{u}})\, \mathrm{d}m$$

cause the inertial loads

$$(10)\quad Q_{v,\mathrm{rot}}^{f,g} = -2\int_V \rho \mathbf{S}_{\mathrm{rot}}^\top \cdot \bar{u}_A \times (\omega \times \dot{\bar{u}})\, \mathrm{d}V$$

on the flexible DoF. Tests with structures similar to rotor blades have revealed that the order of magnitude of $Q_{v,\mathrm{rot}}^{f,g}$ is negligible compared to $Q_{v,\mathrm{rot}}^{f,c}$. Similar to the inertia shape integrals, the terms $Q_{v,\mathrm{tra}}^f$, $Q_{v,\mathrm{rot}}^{f,c}$, and $Q_{v,\mathrm{rot}}^{f,g}$ are volume integrals including the density ρ. Their conversion to 1D integrals based on 2D cross sectional configuration parameters is presented at the end of Appendix A.2.

The refined implementation of inertial loads affecting flexible motion is assessed via computations based on the HART II rotor blade configuration [10]. Figure 4 depicts the equilibrium flexible tip twist $\vartheta_{\mathrm{flex}}$(tip) at nominal rotor speed in vacuo, depending on the blade collective pitch angle $\vartheta_{\mathrm{pre},75}$; the

index 75 denotes the pitch reference of 75% rotor radius. Results are shown for three variants of the inertial loads calculation:

- Baseline: $Q_v^f = Q_{v,\mathrm{tra}}^f$, Equation 6.
- Upgrade 1: $Q_v^f = Q_{v,\mathrm{tra}}^f + Q_{v,\mathrm{rot}}^{f,c} + Q_{v,\mathrm{rot}}^{f,g}$, Equations 6, 8, and 10, but using the undeformed rotation $\mathbf{T} = \mathbf{T}_{\mathrm{ERF}}$ to transform inertial properties into the FFR.
- Upgrade 2: Like upgrade 1, but the flexible deformation is considered when transforming inertial properties into the FFR: $\mathbf{T} = \mathbf{T}_{\mathrm{flex}} \cdot \mathbf{T}_{\mathrm{ERF}}$. Details on this transformation are given in Appendix A.2. This upgrade is important to account for the spring-like effect of the propeller moment: The flexible twist causes a restoring propeller moment, as illustrated in Figure 5.

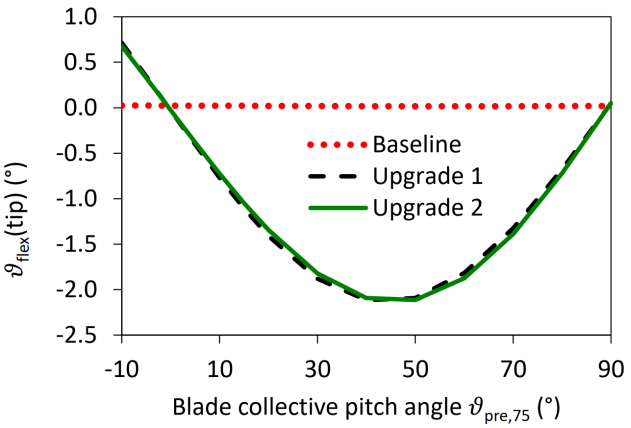

Figure 4: Equilibrium flexible tip twist $\vartheta_{\mathrm{flex}}$(tip) of the HART II rotor blade (stiff root attachment) due to the propeller moment at nominal rotor speed $\Omega = 109\,\mathrm{rad/s}$ in vacuo, calculated using VAST

As expected, the baseline implementation does not model the propeller moment; no significant $\vartheta_{\mathrm{flex}}$(tip) is observed. With upgrade 1, $\vartheta_{\mathrm{flex}}$(tip) is negative for roughly $0° < \vartheta_{\mathrm{pre,75}} < 90°$, with a maximum magnitude at $\vartheta_{\mathrm{pre,75}} \approx 45°$. Since the propeller moment tends to orient the blade flat in the rotor plane of rotation, $\vartheta_{\mathrm{flex}}$(tip) opposes $\vartheta_{\mathrm{pre,75}}$. The magnitude of this flexible twist is overpredicted for $0° < \vartheta_{\mathrm{pre,75}} < 45°$ and underpredicted for $45° < \vartheta_{\mathrm{pre,75}} < 90°$ because the acting inertial loads are still based on the undeformed configuration. Therein, the outboard blade sections are more inclined with respect to the plane of rotation than in the deformed configuration. Upgrade 2 resolves this issue by calculating the inertial loads in the deformed state, i.e. $\mathbf{T}_{\mathrm{flex}}$ (rotation matrix representing $\vartheta_{\mathrm{flex}}$) is taken into account. Details on consideration of $\mathbf{T}_{\mathrm{flex}}$ during the calculation of Q_v^f are presented in Appendix A.2. Note that the flexible twist of upgrade 2 in Figure 4 is solely attributed to inertial loads and does not include the influence of the aerodynamic pitching moment. Therefore, the flexible tip twist of $-0.27°$ (upgrade 2) at $\vartheta_{\mathrm{pre,75}} = 3.8°$ is of smaller magnitude than that of a trimmed wind tunnel setup[10] ($\vartheta_{\mathrm{flex}}(\mathrm{tip}) = -1.09°$), see Table 1.

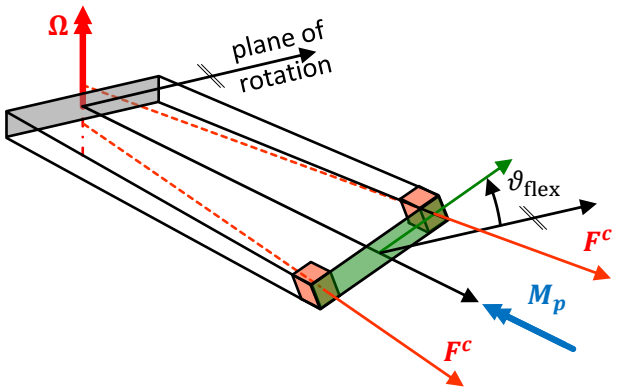

Figure 5: Propeller moment M_p due to *flexible* twist. Root section lies flat in the plane of rotation; tip section is inclined by $\vartheta_{\mathrm{flex}}$ relative to $\vartheta_{\mathrm{pre}} = 0°$

Table 1: Comparison of $\vartheta_{\mathrm{flex}}$(tip) for $\vartheta_{\mathrm{pre,75}} = 3.8°$; VAST calculations in vacuo (*no airloads*)

trim incl. airloads[10]	VAST baseline	VAST upgrade 1	VAST upgrade 2
$-1.09°$	$0.00°$	$-0.29°$	$-0.27°$

Figure 6 shows the Campbell diagram of the HART II rotor blade using the three implementations described above. The only difference between the variants is observed for the first torsional mode T1. Remarkably, upgrade 1 does not change the torsion eigenfrequency compared to the baseline. Both the baseline and upgrade 1 show the same eigenfrequency increase with rising rotor speed, which is attributed to the geometric stiffening. The corresponding terms are part of the stiffness matrix $\mathbf{K}_{ff}$. Aside from this geometric stiffening, the change of the propeller moment M_p with $\vartheta_{\mathrm{flex}}$ causes a further increase in the effective stiffness of the torsion mode. This is the spring-like effect of the propeller moment presented in Figure 5. The feature required to model this effect is upgrade 2, which considers the dependency of inertial loads on deformation. Accordingly, the T1 eigenfrequency increase is even larger with upgrade 2. It should be noted that this further eigenfrequency increase is only observable in the Campbell diagram if the derivative $\partial Q_v^f / \partial r_\mathrm{l}$ is

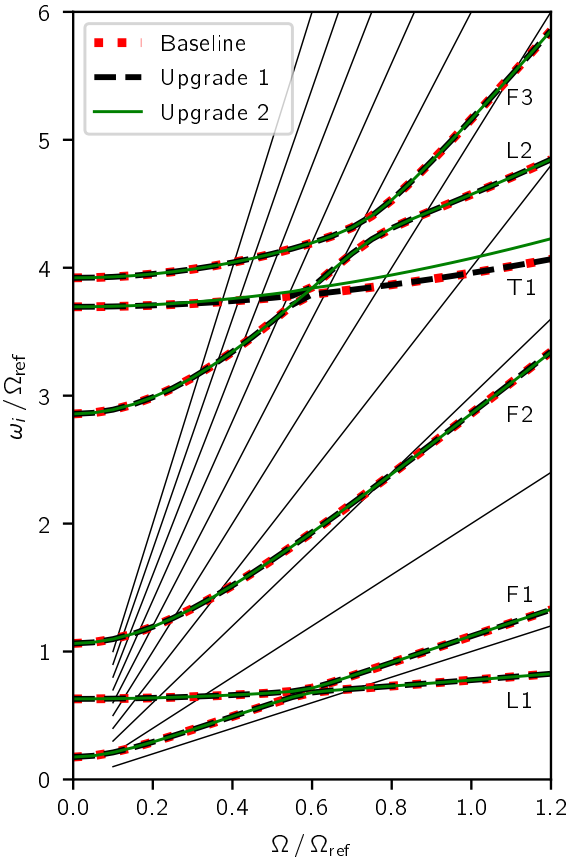

Figure 6: Campbell diagram of the HART II rotor blade (stiff root attachment), calculated using VAST

interpreted as a stiffness term in the modal analysis, as explained in detail in Section 6.

The results of the HART II rotor blade in Figure 4 and Figure 6 are plausible. However, no experimental measurements of the eigenfrequencies of the rotating blade were available for validation. To verify the model, a simpler configuration was analyzed for which the exact reference results were determined analytically. The verification is presented in Appendix A.3.

4. ACCELERATED FFR

The inertial load terms Equation 6 and Equation 8 include the centripetal acceleration $\tilde{\omega}\tilde{\omega}\bar{u} = \omega \times (\omega \times \bar{u})$ which is the most dominant inertial load occuring in rotor dynamics and therefore very important. The vector $\bar{u}$ denotes the location of a particle relative to the FFR. When testing a rotor blade which was attached at a hinge offset e (i.e. the FFR was located outside the rotor center; see Figure 7), the centrifugal loads were underpredicted because in such a configuration, the hinge offset causes a centripetal acceleration $\omega \times (\omega \times e)$ of the FFR which is missing in the baseline dynamic Equation 1. The reason why it is missing is the choice of the coordinate system to express v, which is the FFR itself. An equilibrium with $\Omega = \omega = const.$ implies $\dot{v} = 0$, and consequently the term $\bar{\mathbf{S}}^{\mathsf{T}} \dot{v}$ in the bottom row of Equation 1 vanishes. Therefore, if the FFR's centripetal acceleration is not explicitly respected in Q^f_v (as done in this work; see further below), the centrifugal loads are underpredicted if the FFR is located outside the center of rotation. Note that in [6],

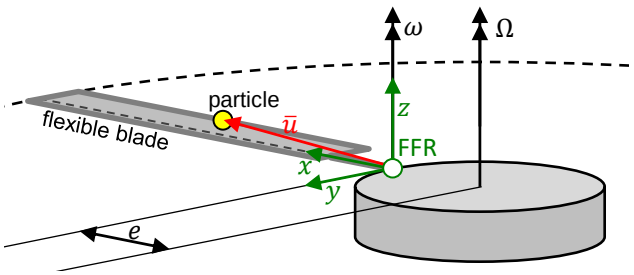

Figure 7: FFR located outside the center of rotation

in contrast to this work, v was chosen to be expressed in the coordinates of the inertial system, so that in the above described equilibrium condition, its derivative resembles the Euler term $\dot{v} = \omega \times v = \omega \times (\omega \times e)$, which is exactly the centripetal acceleration of the FFR. So in [6], this portion of the centrifugal loads is part of the left hand side of the dynamic equation.

To conform to the architectural requirements in the VAST-MBS, however, v shall be expressed in the FFR coordinates. Accordingly, the translatory acceleration a must be added to the inertial loads on the right hand side to appropriately model cases like the one shown in Figure 7. The modified terms are:

$$(11)\quad Q^f_{v,\mathrm{tra}} = -\int_V \rho\, \mathbf{S}^{\mathsf{T}}_{\mathrm{tra}} \left(a + \tilde{\omega}\,\tilde{\omega}\,\bar{u} + 2\,\tilde{\omega}\,\dot{\bar{u}}\right) \mathrm{d}V$$

$$(12)\quad Q^{f,c}_{v,\mathrm{rot}} = -\int_V \rho\, \mathbf{S}^{\mathsf{T}}_{\mathrm{rot}} \cdot \bar{u}_A \times \left(a + \tilde{\omega}\,\tilde{\omega}\,\bar{u}\right) \mathrm{d}V$$

For conversion to 1D integrals see Appendix A.2. Note that a only includes accelerations arising from the states of the MBS, *not* from the state derivatives. The term $\omega \times (\omega \times e)$ is one example for such an acceleration. The motion of all preceding bodies in the kinematic tree of the MBS (e.g. helicopter fuselage and rotor hub) – defined by the MBS' minimal states – is evaluated in VAST to compute a. The left hand side of the MBS' dynamic equation, in contrast, is not needed to calculate a.

The enhanced implementation including a is verified in Appendix A.4, based on analytical reference

results of the axial tip displacement of an aluminum beam attached to a rotating hub with offset e.

5. EXTERNAL LOADS APPLICATION

Besides the inertial loads Q_v, further load terms appear on the right hand side of Equation 1. These are gravitational loads Q_g and external loads Q_e. The effect of gravity g on flexible motion is simply expressed by $Q_g^f = \bar{\mathbf{S}}^\mathsf{T} g$ with $\bar{\mathbf{S}}$ as given in Equation 29 of Appendix A.2. Since $\bar{\mathbf{S}}$ includes the translatory shape functions only, gravity so far only affects the translatory flexible DoF. A direct effect of gravity on rotational flexible DoF, which is expected when the mass axis has an offset from the beam axis, is not modeled yet. However, in most simulation scenarios of helicopter rotor dynamics, gravity loads play a minor role so that this effect is not considered relevant. A remark on wind turbine applications will be given in the outlook, Section 8.

Describing the term Q_e^f based on discrete external loads F_e and M_e, in contrast, is more demanding. These loads may be applied at a marker within

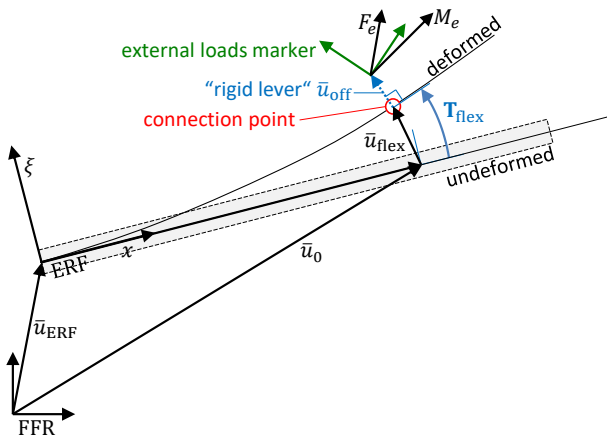

Figure 8: Schematic of external loads application

an element (i.e. *not* at a node of the FE system) and/or with an offset $\bar{u}_{\text{off}}$ from the beam axis, see Figure 8. Such a case can occur, for example, when the structural and aerodynamic discretizations of a rotor blade differ from one another. Since external loads – e.g. airloads – may depend on the motion (position, orientation, velocity, angular velocity) of the marker on which they act, their application requires two calculations which must be consistent, i.e. based on the same transformations:

1. Evaluate the kinematics of the marker based on that of the flexible beam: A loads marker as shown in Figure 8 is configured and handled the following way in VAST. On the nearest element of the FE system, a connection point is defined on the beam axis such that $|\bar{u}_{\text{off}}|$ is minimal. The offset vector $\bar{u}_{\text{off}}$ is considered invariant, so the loads marker moves as if it was connected by a "rigid lever" to the connection point. The connection point, in turn, moves in space according to the FFR motion (rigid body part) and the flexible motion of the beam (e.g. flexible displacement $\bar{u}_{\text{flex}}$). The latter is evaluated based on the states $r_|$ and $r_{||}$ of the beam, along with the shape function evaluations $\mathbf{S}_{\text{tra}}(x)$, $\mathbf{S}_{\text{rot}}(x)$ at the location x of the connection point. For instance, the flexible translatory displacement reads

$$\bar{u}_{\text{flex}}(x) = \mathbf{S}_{\text{tra}}(x) \cdot r_| . \tag{13}$$

In VAST, Equation 13 is evaluated element-wise, i.e. the element's shape function is multiplied with only those nodal states that belong to the element. The loads marker position relative to the FFR is $\bar{u} = \bar{u}_0 + \bar{u}_{\text{flex}} + \bar{u}_{\text{off}}$. The rotation from the FFR to the marker frame is composed of $\mathbf{T} = \mathbf{T}_{\text{flex}} \cdot \mathbf{T}_{\text{mark}} \cdot \mathbf{T}_{\text{ERF}}$, where $\mathbf{T}_{\text{mark}}$ is the rotation from the ERF to the loads marker frame in the undeformed configuration and $\mathbf{T}_{\text{flex}}$ is a matrix representing the flexible rotations $\mathbf{S}_{\text{rot}}(x) \cdot r_|$.

2. Project the loads onto the nodal deflections: The force acting at the connection point is identical to that acting at the external loads marker. The effective moment at the connection point, in contrast, additionally includes the influence of the force's lever arm (superscript *):

$$M_e^* = M_e + \bar{u}_{\text{off}} \times F_e \tag{14}$$

The nodal loads Q_e^f are obtained by multiplication with the shape functions of the elements:

$$Q_{e,\text{tra}}^f = \mathbf{S}_{\text{tra}}^\mathsf{T} \cdot F_e \tag{15}$$
$$Q_{e,\text{rot}}^f = \mathbf{S}_{\text{rot}}^\mathsf{T} \cdot M_e^* \tag{16}$$

Note that the loads F_e and M_e^* are expressed in the coordinates of the FFR, which requires a preceding transformation (multiplication by $\mathbf{T}^\mathsf{T}$) if the loads were expressed in the external loads marker frame. Details on coordinate transformations are provided in Appendix A.1. In VAST, Equations 15 and 16 are evaluated only for the finite element which is affected by F_e and M_e^*. Accordingly, $Q_{e,\text{tra}}^f$ and $Q_{e,\text{rot}}^f$ are then placed in the appropriate segment of Q_e^f in Equation 1 belonging to this element.

The application of external loads is verified based on analytical reference calculations in Appendix A.5. Both the effect of eccentric forces and the application of forces within an element, i.e. between the nodes, are addressed.

6. MODAL REDUCTION

The goal of modal reduction is to limit the kinematics of the system to pre-defined modes. The number of states is reduced and the differential equations become numerically less “stiff”. This allows the usage of standard solvers like Runge-Kutta with reasonable time steps. For a flexible system without damping, the eigenvalue problem is given by

$$\left(\mathbf{K}^*_{\text{free}} - \omega_i^2 \mathbf{M}_{\text{free}}\right) u_{\text{free},i} = 0. \tag{17}$$

The subscript “free” indicates that the matrices or vectors are reduced to the number of free DoF. The locked DoF of the boundary conditions are removed, e.g. $\mathbf{M}_{\text{free}} = \mathbf{J}_{\text{DoF}}^{\top} \mathbf{M}_{ff} \mathbf{J}_{\text{DoF}}$. $\mathbf{J}_{\text{DoF}}$ contains rows of the identity matrix for the free DoF and rows of zeros for the locked degrees of freedom. The boundary conditions are customizable. For a hingeless rotor blade, for instance, a clamped boundary condition of the first node with respect to the FFR is used. The extended stiffness matrix $\mathbf{K}^*_{\text{free}}$ includes the free stiffness matrix $\mathbf{K}_{\text{free}} = \mathbf{J}_{\text{DoF}}^{\top} \mathbf{K}_{ff} \mathbf{J}_{\text{DoF}}$ as well as an additional Jacobian which is explained further below.

ω_i is one of the FE system’s eigenfrequencies, and $u_{\text{free},i}$ is the eigenvector of the free DoF corresponding to ω_i. Only the first n eigenmodes $i = 1 \ldots n$ of the FE system are used to describe its motion, while n is configurable. n modal coordinates imply n position level states and n velocity level states. Accordingly, the $2n$ flexible states are factors scaling the eigenvectors $u_i = \mathbf{J}_{\text{DoF}}\, u_{\text{free},i}$ to obtain the FE system’s deflections r_{f} and deflection velocities $r_{\text{f}\dot{}}$. The flexible part of Equation 1 – i.e. the lower half – is projected onto the modal base and the modal coordinates replace the flexible states $(r_{\text{f}}, r_{\text{f}\dot{}})$ in the solution process.

When calculating the modal reduction, the motion of the FFR must be taken into account, since it actively affects the system’s eigenfrequencies. Therefore, an addition to the stiffness matrix $\mathbf{K}_{\text{free}}$ in the form of a derivative of the inertial loads Q_v^f is considered.

First, the FE system is brought to an equilibrium state under the interial loads Q_v^f, resulting from the motion of the FFR. Consequently, the stiffness matrix $\mathbf{K}_{ff}$ is calculated, potentially including geometric stiffening terms. Furthermore, the inertial loads on free flexible motion $Q^f_{v,\text{free}} = \mathbf{J}_{\text{DoF}}^{\top} Q_v^f$ are derived with respect to the free flexible position level states $r_{\text{f,free}} = \mathbf{J}_{\text{DoF}}^{\top} r_{\text{f}}$ by means of finite differences. The resulting Jacobian is superimposed onto the stiffness matrix in Equation 18. The negative sign is attributed to the fact that the stiffness term $-\mathbf{K}_{ff}\, r_{\text{f}}$ also appears with negative sign in Equation 1.

$$\mathbf{K}^*_{\text{free}} = \mathbf{K}_{\text{free}} - \partial Q^f_{v,\text{free}} / \partial r_{\text{f,free}} \tag{18}$$

In other words, the dependency of the flexible inertial right hand side on the flexible displacements is interpreted as an additional stiffness for the modal reduction. This step is necessary, for example, to obtain correct lead-lag eigenmodes of rotor blades, because the direction of the centrifugal force vector on a mass increment of the blade changes immediately when the blade lags. Without the consideration of $\partial Q^f_{v,\text{free}} / \partial r_{\text{f,free}}$, the lead-lag eigenfrequency would be too high, since the stiffening effect would be similar to that of the flap modes for which the centrifugal force vector does not change its direction when the blade flaps. So $\partial Q^f_{v,\text{free}} / \partial r_{\text{f,free}}$ provides a negative stiffness in this case.

A comparison between eigenfrequencies of the modal reduction based on $\mathbf{K}_{\text{free}}$ only, and the modification based on $\mathbf{K}^*_{\text{free}}$ according to Equation 18, is given in Table 2. It lists the eigenfrequencies of the first six modes of the HART II rotor blade with stiff root attachment at nominal rotor speed $\Omega_{\text{ref}} = 109\,\text{rad/s}$.

Table 2: Normalized eigenfrequencies $\omega_i/\Omega_{\text{ref}}$ of the HART II rotor blade (stiff root attachment) at nominal rotor speed $\Omega = 109\,\text{rad/s}$. In **red**: over-/ underpredicted values

	stiffness for modal reduction		
mode	$\mathbf{K}_{\text{free}}$ only	$\mathbf{K}^*_{\text{free}}$ (Equation 18)	
L1	**1.27**	**0.78**	(↓)
F1	1.12	1.10	
F2	2.86	2.85	
T1	**3.96**	**4.04**	(↑)
L2	**4.68**	**4.57**	(↓)
F3	5.16	5.16	

The eigenfrequencies of the modified implementation resemble those of “upgrade 2” in Figure 6 at $\Omega/\Omega_{\text{ref}} = 1$. Without consideration of $\partial Q^f_{v,\text{free}} / \partial r_{\text{f,free}}$, the lead-lag eigenfrequencies – especially that of L1 – are significantly overpredicted; a value of $\omega_{\text{L1}}/\Omega_{\text{ref}} = 1.27$ characterizes a very stiff-in-plane rotor, while the HART II rotor is of the soft-in-plane type. The explanation based on the centrifugal force vector has already been given above.

In contrast to the lead-lag modes, the first torsion mode T1 is underpredicted if only $\mathbf{K}_{\text{free}}$ is considered for modal reduction. The reason is the missing spring-like effect of the propeller moment (see Section 3), which is included in $\partial Q^f_{v,\text{free}}/\partial r_{\text{I},\text{free}}$. The flap modes F1, F2 and F3 are barely affected by the added Jacobian in Equation 18. The very small decreases of the F1 and F2 eigenfrequencies can be explained by secondary lead-lag contributions in these modes.

It should be mentioned that the dependency on velocity level states $\partial Q^f_{v,\text{free}}/\partial r_{\text{II},\text{free}}$ is not considered because it would need to be interpreted as damping, which is neglected in the modal reduction calculation. Therefore, if precise eigenfrequencies and damping characteristics are to be calculated (e.g. in a Campbell diagram), a VAST-wide modal analysis is performed, in which the complete differential equations of the MBS are linearized including all damping and right hand side terms.

7. CONCLUSION

The FFR-based integration of FE bodies in the MBS of VAST is completed in its first version using BAM finite elements. During implementation and concurrent testing, enhancements were added to make the simulation model suitable for rotorcraft applications. These enhancements include:

- the configuration of inertial properties based on 2D cross sectional data instead of the 3D density distribution,
- the introduction of rotational shape functions to account e.g. for the propeller moment,
- the consideration of an accelerated FFR to address the blade attachment's radial offset from the rotor center in the centrifugal field,
- the handling of external loads (e.g. airloads) that are applied away from the beam's nodes or the beam axis to allow for independent structural and aerodynamic discretization, and
- the dependency of inertial loads on flexible position level states as an additional stiffness which is considered during modal reduction.

The modifications were verified against analytical reference results for appropriate rotor dynamics test cases. Plausible tip twist and Campbell diagram results were presented for the HART II rotor blade. This paper therefore provides necessary modifications to make the well-known FFR formulation capable of simulating helicopter rotor blades as FE beams in an MBS environment.

8. OUTLOOK

Because the test cases studied in this paper only feature clamped beam attachments, the coupling between the rigid body motion and the flexible motion of the body has not yet been verified. This coupling is modeled by the matrices $\bar{\mathbf{S}}$ and $\bar{\mathbf{J}}_{\theta f}$, which are so far solely based on translatory shape functions $\mathbf{S}_{\text{tra}}$. Currently, the consideration of rotational shape functions $\mathbf{S}_{\text{rot}}$ in $\bar{\mathbf{S}}$, in $\bar{\mathbf{J}}_{\theta f}$, and in the FE system's mass matrix $\mathbf{M}_{ff}$ is being investigated. Since $\bar{\mathbf{S}}$ also affects gravitational loads Q^f_g, the modification of $\bar{\mathbf{S}}$ is also expected to be relevant for wind turbine simulations, where gravity causes a major cyclic excitation on the turbine's blades.

In the near future, in addition to the static and frequency domain analyses presented in this paper, comprehensive tests based on time domain simulations such as wind tunnel trim calculations or transient responses are planned. To address nonlinear effects of deformation (e.g. part of the Coriolis coupling between flap and lead-lag motion), the substructuring approach will be employed, i.e. the rotor blade will be segmented into multiple linear FE bodies. Code refactoring and performance improvements are also included in the short-term agenda.

In the mid-term, the VAST-MBS will be extended to model closed-loop structures such as dual load paths, which occur e.g. when the blade root pitch actuation is explicitly modeled and/or the rotor blade has a bearingless attachment.

The long-term added value of modeling rotor blades as FE beams within the VAST-MBS is the ability to accurately and efficiently simulate

- flexible rotor blades with complex geometrical and structural properties as well as arbitrary boundary conditions,
- complete structural systems with flexible rotors coupled to moving and/or vibrating vehicles and drive systems, and
- dedicated multi body structures for the blade attachment including hinges, rigid connections, flexible elements, springs and dampers.

ACKNOWLEDGMENTS

The authors would like to thank all members of the VAST developer team for their great collaboration. Each individual contributed their effort towards realizing the achievements presented in this paper. Particular thanks are due to Maximilian Mindt for

his thorough literature review and advice related to the propeller moment. Furthermore, the support from Rémi Coisnon and Yan Skladanek at Airbus Helicopters for integrating BAM into VAST is greatly appreciated.

References

[1] Hofmann, J., Weiss, F., and Mindt, M., "A New Approach to Comprehensive Rotorcraft Aeromechanics Simulation," *VFS 77th Annual Forum and Technology Display*, Online, May 2021.

[2] Kontak, M., Röhrig-Zöllner, M., Hofmann, J., and Weiß, F., "Automatic Differentiation in Multibody Helicopter Simulation," *Multibody Dynamics 2019*, edited by A. Kecskeméthy and F. Geu Flores, Vol. 53, Springer International Publishing, Cham, 2020, pp. 534–542.

[3] Skladanek, Y., *Formulation d'un élément fini de poutre pour la dynamique des pales d'hélicoptère de géométrie complexe*, Ph.D. thesis, l'Institut National des Sciences Appliquées de Lyon, France, 2011.

[4] Skladanek, Y., Cranga, P., Ferraris, G., Jacquet, G., and Dufour, R., "A Highly Accurate Beam Finite Element for Curved and Twisted Helicopter Blades," *ASME 2011 International Design Engineering Technical Conferences and Computers and Information in Engineering Conference*, Washington, D.C., Aug. 2011.

[5] Skladanek, Y., Boucherie, L., Benoit, B., and Cranga, P., "Advanced beam modeling applied to articulated rotor – Implementation in HOST aeromechanic simulation tool," *AHS 70th Annual Forum and Technology Display*, Montréal, Québec, Canada, May 2014.

[6] Shabana, A. A., *Dynamics of multibody systems*, Cambridge University Press, Cambridge, 2005.

[7] Schiavo, F., Ferretti, G., and Vigano, L., "Object-Oriented Modelling and Simulation of Flexible Multibody Thin Beams in Modelica with the Finite Element Method," *4th International Modelica Conference*, Hamburg, Germany, March 2005.

[8] Johnson, W., *Rotorcraft Aeromechanics*, Cambridge University Press, Cambridge, 2013.

[9] Bielawa, R. L., *Rotary Wing Structural Dynamics and Aeroelasticity*, American Institute of Aeronautics and Astronautics, Reston, VA, 2nd ed., 2006.

[10] van der Wall, B. G., Lim, J. W., Smith, M. J., Jung, S. N., Bailly, J., Baeder, J. D., and Boyd, D. D., "The HART II international workshop: an assessment of the state-of-the-art in comprehensive code prediction," *CEAS Aeronautical Journal*, Vol. 4, No. 3, Sept. 2013, pp. 223–252.

[11] Houbolt, J. C. and Brooks, G. W., "Differential Equations of Motion for Combined Flapwise Bending, Chordwise Bending, and Torsion of Twisted Nonuniform Rotor Blades," NACA TR 1346, Washington, D.C., 1958.

[12] Roark, R. J., Young, W. C., and Budynas, R. G., *Roark's formulas for stress and strain*, McGraw-Hill, New York, 7th ed., 2002.

A. APPENDICES

A.1. Coordinate Transformations

Throughout this paper, transformations are needed which rotate vectors or matrices from the FFR into a specific frame or vice verca, i.e. the transformations change the coordinate system in which a quantity is expressed. If not indicated explicitly, quantities are expressed in the FFR by convention. 3D vectors $v^{(\mathrm{mark})}$ and 3×3 matrices $\mathbf{M}^{(\mathrm{mark})}$ that are expressed in a specific marker frame – indicated by superscript (mark) – are obtained as follows from the FFR-expressed quantities

$$v^{(\mathrm{mark})} = \mathbf{T} \cdot v \tag{19}$$

$$\mathbf{M}^{(\mathrm{mark})} = \mathbf{T} \cdot \mathbf{M} \cdot \mathbf{T}^{\top}, \tag{20}$$

where $\mathbf{T}$ is a 3×3 rotation matrix. The other way around, FFR-expressed quantities are obtained as

$$v = \mathbf{T}^{\top} \cdot v^{(\mathrm{mark})} \tag{21}$$

$$\mathbf{M} = \mathbf{T}^{\top} \cdot \mathbf{M}^{(\mathrm{mark})} \cdot \mathbf{T}. \tag{22}$$

$\mathbf{T}$ may be composed of several subsequent rotations. For example, in Figure 8, the rotation from the FFR to the marker frame is composed of $\mathbf{T} = \mathbf{T}_{\mathrm{flex}} \cdot \mathbf{T}_{\mathrm{mark}} \cdot \mathbf{T}_{\mathrm{ERF}}$. The individual rotations are explained in Section 5.

Since the individual entries of the nodal states $r_{|}$ and $r_{||}$ belonging to an element can be associated with the three spatial directions, a rotation matrix $\mathbb{T}$ can be defined in analogy to $\mathbf{T}$ which transforms the element's nodal states from the FFR to the ERF. For instance, $\mathbb{T}$ is used along with $\mathbf{T}$ to rotate the shape function matrices – which are originally defined in the ERF – into the FFR:

$$\mathbf{S}_{\mathrm{tra}} = \mathbf{T}^{\top} \cdot \mathbf{S}_{\mathrm{tra}}^{(\mathrm{ERF})} \cdot \mathbb{T} \tag{23}$$

$$\mathbf{S}_{\mathrm{rot}} = \mathbf{T}^{\top} \cdot \mathbf{S}_{\mathrm{rot}}^{(\mathrm{ERF})} \cdot \mathbb{T} \tag{24}$$

A.2. 1D Inertia Shape Integrals

This detailed derivation of 1D inertia shape integrals is given here. In [6] and [7], the 3D inertia shape integrals over the body volume V are derived, based on density ρ and translatory shape function matrices $\mathbf{S}_{\text{tra}}$. These integrals are computed for the whole FE system with its n_r flexible DoF and are expressed in the coordinates of the FFR. The dynamic Equation 1 of the FE body includes most of the integrals, which read:

(25)	$\mathbf{m}_{RR} = \int_V \rho\, \mathbf{I}\, \mathrm{d}V$	3×3	rigid translatory mass matrix
(26)	$\bar{\mathbf{J}}_{\theta\theta} = \int_V \rho\, \tilde{\bar{u}}^{\mathsf{T}}\, \tilde{\bar{u}}\, \mathrm{d}V$	3×3	rigid rotational inertia tensor
(27)	$\tilde{\bar{\mathbf{S}}}_t = \int_V \rho\, \tilde{\bar{u}}\, \mathrm{d}V$	3×3	rigid transl./rigid rot. coupling matrix
(28)	$\mathbf{M}_{ff} = \int_V \rho\, \mathbf{S}_{\text{tra}}^{\mathsf{T}}\, \mathbf{S}_{\text{tra}}\, \mathrm{d}V$	$n_r \times n_r$	mass matrix of the FE system
(29)	$\bar{\mathbf{S}} = \int_V \rho\, \mathbf{S}_{\text{tra}}\, \mathrm{d}V$	$3 \times n_r$	rigid transl./flex. coupling matrix
(30)	$\bar{\mathbf{J}}_{\theta f} = \int_V \rho\, \tilde{\bar{u}}\, \mathbf{S}_{\text{tra}}\, \mathrm{d}V$	$3 \times n_r$	rigid rot./flex. coupling matrix

The aim is to obtain the inertia shape integrals via 1D integration using pre-evaluated 2D cross-sectional integrals as the configuration input. Note that the integration space itself always represents the undeformed beam and does not change due to deformation. Figure 2 shows the schematic of a beam with the vectors and rotations described in the following. The vector $\bar{u}$ from the FFR to a particle of the beam, expressed in the FFR, is obtained as follows:

$$\text{(31)} \qquad \bar{u} = \underbrace{\bar{u}_0 + \overbrace{\mathbf{T}_{\text{ERF}}^{\mathsf{T}} \cdot \left(\mathbf{S}_{\text{tra}}^{(\text{ERF})} \cdot r_l^{(\text{ERF})}\right)}^{\bar{u}_{\text{flex}}}}_{\bar{u}_m} + \underbrace{\mathbf{T}_{\text{ERF}}^{\mathsf{T}} \cdot \bar{u}_A^{(\text{ERF})}}_{\bar{u}_A} \quad \text{with}$$

$\bar{u}_0$ = undeformed position on the beam axis, expressed in the FFR

$\mathbf{T}_{\text{ERF}}^{\mathsf{T}}$ = matrix to rotate a vector from the ERF to the FFR

$\mathbf{S}_{\text{tra}}^{(\text{ERF})}$ = translatory shape function matrix, expressed in the ERF

$r_l^{(\text{ERF})}$ = element-related position-level states, expressed in the ERF

$\bar{u}_{\text{flex}}$ = flexible deformation, expressed in the FFR

$\bar{u}_m$ = deformed position on the beam axis, expressed in the FFR

$\bar{u}_A^{(\text{ERF})}$ = offset from beam axis within the cross section, expressed in the ERF

$\bar{u}_A$ = offset from beam axis within the cross section, expressed in the FFR

The reformulation of the rigid translatory mass matrix is trivial. It is obtained by integrating the cross-section moment I_{00} along the beam. $\mathbf{I}$ denotes the identity matrix.

$$\text{(32)} \qquad \mathbf{m}_{RR} = \int_V \rho\, \mathbf{I}\, \mathrm{d}V = \mathbf{I} \cdot \int_x \underbrace{\int_A \rho\, \mathrm{d}A}_{I_{00}}\, \mathrm{d}x$$

The inertia tensor is reformulated as follows. Note that the vector $\bar{u}_m$ from the FFR to the origin of the local coordinate system is constant during the integration over A, so it can be taken outside of the integral.

$$
\begin{aligned}
(33)\quad \bar{\mathbf{J}}_{\theta\theta} &= \int_V \rho\, \tilde{\bar{u}}^{\mathsf{T}}\, \tilde{\bar{u}}\, \mathrm{d}V = \int_x \int_A \rho \tilde{\bar{u}}^{\mathsf{T}}\, \tilde{\bar{u}}\, \mathrm{d}A\, \mathrm{d}x = \int_x \int_A \rho \widetilde{(\bar{u}_m + \bar{u}_A)}^{\mathsf{T}}\, \widetilde{(\bar{u}_m + \bar{u}_A)}\, \mathrm{d}A\, \mathrm{d}x \\
&= \int_x \left[\int_A \rho \tilde{\bar{u}}_m^{\mathsf{T}}\, \tilde{\bar{u}}_m\, \mathrm{d}A + \int_A \rho \left(\tilde{\bar{u}}_m^{\mathsf{T}}\, \tilde{\bar{u}}_A + \tilde{\bar{u}}_A^{\mathsf{T}}\, \tilde{\bar{u}}_m \right) \mathrm{d}A + \int_A \rho \tilde{\bar{u}}_A^{\mathsf{T}}\, \tilde{\bar{u}}_A\, \mathrm{d}A \right] \mathrm{d}x \\
&= \int_x \left[\tilde{\bar{u}}_m^{\mathsf{T}}\, \tilde{\bar{u}}_m \underbrace{\int_A \rho\, \mathrm{d}A}_{I_{00}} + \tilde{\bar{u}}_m^{\mathsf{T}} \int_A \rho \tilde{\bar{u}}_A\, \mathrm{d}A + \int_A \rho \tilde{\bar{u}}_A^{\mathsf{T}}\, \mathrm{d}A\, \tilde{\bar{u}}_m + \int_A \rho \tilde{\bar{u}}_A^{\mathsf{T}}\, \tilde{\bar{u}}_A\, \mathrm{d}A \right] \mathrm{d}x
\end{aligned}
$$

If the vector $\bar{u}_A$ is expressed in the ERF, it reads $\bar{u}_A^{(\mathrm{ERF})} = (0, \xi, \eta)^{\mathsf{T}}$ since the plane A is perpendicular to the beam axis. Accordigly, the local inertia per length is

$$
(34)\quad \int_A \rho \tilde{\bar{u}}_A^{(\mathrm{ERF})^{\mathsf{T}}}\, \tilde{\bar{u}}_A^{(\mathrm{ERF})}\, \mathrm{d}A = \int_A \rho \begin{pmatrix} \xi^2 + \eta^2 & 0 & 0 \\ 0 & \eta^2 & -\xi\,\eta \\ 0 & -\xi\,\eta & \xi^2 \end{pmatrix} \mathrm{d}A = \begin{pmatrix} I_{20} + I_{02} & 0 & 0 \\ 0 & I_{02} & -I_{11} \\ 0 & -I_{11} & I_{20} \end{pmatrix}
$$

with $I_{20} = \int_A \rho\, \xi^2\, \mathrm{d}A$, $I_{02} = \int_A \rho\, \eta^2\, \mathrm{d}A$, and $I_{11} = \int_A \rho\, \xi\, \eta\, \mathrm{d}A$. Furthermore, the matrix

$$
(35)\quad \int_A \rho \tilde{\bar{u}}_A^{(\mathrm{ERF})}\, \mathrm{d}A = \int_A \rho \begin{pmatrix} 0 & -\eta & \xi \\ \eta & 0 & 0 \\ -\xi & 0 & 0 \end{pmatrix} \mathrm{d}A = \begin{pmatrix} 0 & -I_{01} & I_{10} \\ I_{01} & 0 & 0 \\ -I_{10} & 0 & 0 \end{pmatrix}
$$

is identified, containing the 1st order cross-section moments $I_{10} = \int_A \rho\, \xi\, \mathrm{d}A$ and $I_{01} = \int_A \rho\, \eta\, \mathrm{d}A$.

The inertia shape integrals are expressed in the FFR. In general, the given cross-section moments are expressed in a different, local coordinate system indicated by superscript$^{(\mathrm{local})}$ which requires a coordinate transformation including two steps: The matrix $\mathbf{T}_{\mathrm{ERF}}$ describes the orientation of the ERF relative to the FFR in the undeformed FE system, while the rotation $\mathbf{T}_{\mathrm{flex}}$ accounts for the changed orientation of the local system relative to the ERF due to deformation (cf. Figure 2). The necessity of considering $\mathbf{T}_{\mathrm{flex}}$ during the transformation of the inertia shape integrals was identified in the test cases reported in Section 3. Therein, the implementation including $\mathbf{T}_{\mathrm{flex}}$ is denoted “Upgrade 2,” while “Upgrade 1” does *not* include the rotation $\mathbf{T}_{\mathrm{flex}}$. The total rotation from the FFR to the local deformed coordinate system is described by the matrix $\mathbf{T} = \mathbf{T}_{\mathrm{flex}} \cdot \mathbf{T}_{\mathrm{ERF}}$. The FFR-expressed vectors and matrices are obtained as follows. Further information on coordinate transformations is given in Appendix A.1.

$$
(36)\quad \int_A \rho \bar{u}_A\, \mathrm{d}A = \mathbf{T}^{\mathsf{T}} \cdot \begin{pmatrix} 0 \\ I_{10} \\ I_{01} \end{pmatrix}^{(\mathrm{local})}
$$

$$
(37)\quad \int_A \rho \tilde{\bar{u}}_A\, \mathrm{d}A = \mathbf{T}^{\mathsf{T}} \cdot \begin{pmatrix} 0 & -I_{01} & I_{10} \\ I_{01} & 0 & 0 \\ -I_{10} & 0 & 0 \end{pmatrix}^{(\mathrm{local})} \cdot \mathbf{T}
$$

$$
(38)\quad \int_A \rho \tilde{\bar{u}}_A^{\mathsf{T}}\, \tilde{\bar{u}}_A\, \mathrm{d}A = \mathbf{T}^{\mathsf{T}} \cdot \begin{pmatrix} I_{20} + I_{02} & 0 & 0 \\ 0 & I_{02} & -I_{11} \\ 0 & -I_{11} & I_{20} \end{pmatrix}^{(\mathrm{local})} \cdot \mathbf{T}
$$

Now the coupling matrix $\tilde{\bar{\mathbf{S}}}_t$ between translatory and rotational motion shall be addressed. It is sufficient to transform the term $\bar{\mathbf{S}}_t = \int_V \rho\, \bar{u}\, \mathrm{d}V$ to 1D from; the cross product operation (tilde) is trivial.

$$
\begin{aligned}
(39)\quad \bar{\mathbf{S}}_t &= \int_V \rho\, \bar{u}\, \mathrm{d}V = \int_x \int_A \rho\, \bar{u}\, \mathrm{d}A\, \mathrm{d}x = \int_x \int_A \rho\, (\bar{u}_m + \bar{u}_A)\, \mathrm{d}A\, \mathrm{d}x \\
&= \int_x \left[\bar{u}_m \cdot \underbrace{\int_A \rho\, \mathrm{d}A}_{I_{00}} + \int_A \rho\, \bar{u}_A\, \mathrm{d}A \right] \mathrm{d}x = \int_x \left[\bar{u}_m \cdot I_{00} + \int_A \rho \cdot \mathbf{T}^\top \cdot \begin{pmatrix} 0 \\ \xi \\ \eta \end{pmatrix} \mathrm{d}A \right] \mathrm{d}x \\
&= \int_x \left[\bar{u}_m \cdot I_{00} + \mathbf{T}^\top \cdot \begin{pmatrix} 0 \\ I_{10} \\ I_{01} \end{pmatrix} \right] \mathrm{d}x
\end{aligned}
$$

Again, the vector $(0,\, I_{10},\, I_{01})^\top$ has been transformed from the deformed local frame to the FFR by $\mathbf{T}^\top$.

The rest of the inertia shape integrals includes the translatory shape function matrix $\mathbf{S}_{\mathrm{tra}}$. In the case of beams, the evaluation of the shape function only depends on the distance x along the beam axis. That means that the terms $\mathbf{S}_{\mathrm{tra}}$ and $\mathbf{S}_{\mathrm{tra}}^\top \mathbf{S}_{\mathrm{tra}}$ can always be taken outside of the integration over the cross section. This simplifies the expressions for $\mathbf{M}_{ff}$, $\bar{\mathbf{S}}$ and $\bar{\mathbf{J}}_{\theta f}$ (the latter given in Equation 4 of Section 2):

$$
(40)\quad \mathbf{M}_{ff} = \int_V \rho\, \mathbf{S}_{\mathrm{tra}}^\top \mathbf{S}_{\mathrm{tra}}\, \mathrm{d}V = \int_x \left[\mathbf{S}_{\mathrm{tra}}^\top \mathbf{S}_{\mathrm{tra}} \cdot \underbrace{\int_A \rho\, \mathrm{d}A}_{I_{00}} \right] \mathrm{d}x
$$

$$
(41)\quad \bar{\mathbf{S}} = \int_V \rho\, \mathbf{S}_{\mathrm{tra}}\, \mathrm{d}V = \int_x \left[\mathbf{S}_{\mathrm{tra}} \cdot \underbrace{\int_A \rho\, \mathrm{d}A}_{I_{00}} \right] \mathrm{d}x
$$

Although it is not an "inertia shape integral", the inertial flexible right hand side Q_v^f contains mass integrals, and shall be expressed in 1D form analogously. Note that the angular velocity ω of the FFR is constant over the whole integration domain. For a beam model, the shape function matrix $\mathbf{S}_{\mathrm{tra}}$ does not vary across the beam section so it can be taken outside of the area integral below. Details on the translatory and rotational part $Q_v^f = Q_{v,\mathrm{tra}}^f + Q_{v,\mathrm{rot}}^f$ are treated in Section 3. The translatory acceleration a of the FFR is explicitly considered in Section 4. Considering $\ddot{u} = \ddot{u}_{\mathrm{flex}}$, the translatory inertial loads term can be reformulated as follows:

$$
\begin{aligned}
(42)\quad Q_{v,\mathrm{tra}}^f &= -\int_V \rho\, \mathbf{S}_{\mathrm{tra}}^\top \left(a + \tilde{\omega}\, \tilde{\omega}\, \bar{u} + 2\, \tilde{\omega}\, \dot{\bar{u}} \right) \mathrm{d}V \\
&= -\int_x \left[\mathbf{S}_{\mathrm{tra}}^\top \int_A \rho\, \left(a + \tilde{\omega}\, \tilde{\omega}\, \bar{u} + 2\, \tilde{\omega}\, \dot{\bar{u}} \right) \mathrm{d}A \right] \mathrm{d}x \\
&= -\int_x \left[\mathbf{S}_{\mathrm{tra}}^\top \left(a \int_A \rho\, \mathrm{d}A + \tilde{\omega}\, \tilde{\omega} \int_A \rho\, \bar{u}\, \mathrm{d}A + 2\, \tilde{\omega} \int_A \rho\, \dot{\bar{u}}\, \mathrm{d}A \right) \right] \mathrm{d}x \\
&\overset{\text{cf. Equation 5}}{=} -\int_x \left[\mathbf{S}_{\mathrm{tra}}^\top \left(a \cdot I_{00} + \tilde{\omega}\, \tilde{\omega} \left[\bar{u}_m \cdot I_{00} + \mathbf{T}^\top \cdot \begin{pmatrix} 0 \\ I_{10} \\ I_{01} \end{pmatrix} \right] + 2\, \tilde{\omega}\, \dot{\bar{u}}_{\mathrm{flex}}\, I_{00} \right) \right] \mathrm{d}x
\end{aligned}
$$

Again, the vector $(0, I_{10}, I_{01})^\mathsf{T}$ containing the cross-section moments has been transformed from the local deformed frame to the FFR by $\mathbf{T}^\mathsf{T}$.

The rotational part $Q^f_{v,\mathrm{rot}} = Q^{f,c}_{v,\mathrm{rot}} + Q^{f,g}_{v,\mathrm{rot}}$ is derived for centrifugal (superscript c) and gyroscopic (superscript g) loads separately. Note that $\bar{u} = \bar{u}_m + \bar{u}_A$, and $\omega = (\omega_x, \omega_y, \omega_z)^\mathsf{T}$. The effect of centrifugal loads on the flexible rotational DoF is:

$$
\begin{aligned}
(43)\quad Q^{f,c}_{v,\mathrm{rot}} &= \int_V \rho\, \mathbf{S}^\mathsf{T}_{\mathrm{rot}} \left[-\bar{u}_A \times (a + \omega \times (\omega \times \bar{u}))\right] \mathrm{d}V \\
&= -\int_x \mathbf{S}^\mathsf{T}_{\mathrm{rot}} \int_A \rho \cdot \bar{u}_A \times (a + \omega \times (\omega \times \bar{u}))\, \mathrm{d}A\, \mathrm{d}x \\
&= -\int_x \mathbf{S}^\mathsf{T}_{\mathrm{rot}} \int_A \rho \left[\bar{u}_A \times (a + \omega \times (\omega \times \bar{u}_m)) + \bar{u}_A \times (\omega \times (\omega \times \bar{u}_A))\right] \mathrm{d}A\, \mathrm{d}x \\
&= -\int_x \mathbf{S}^\mathsf{T}_{\mathrm{rot}} \left[\int_A \rho \cdot \bar{u}_A\, \mathrm{d}A \times (a + \omega \times (\omega \times \bar{u}_m)) + \int_A \rho \cdot \underbrace{\bar{u}_A \times (\omega \times (\omega \times \bar{u}_A))}_{\text{triple cross product}} \mathrm{d}A \right] \mathrm{d}x
\end{aligned}
$$

To isolate cross-sectional moments (which are expressed in terms of ρ and $\bar{u}_A$ only) in the second cross-sectional integral above, the triple cross product must be evaluated. Note that the vectors ω and $\bar{u}_A$ must be expressed in the same frame; the FFR is chosen here. The first entry of $\bar{u}_A$ only vanishes if $\bar{u}_A$ is expressed in the ERF: $\bar{u}_A^{(\mathrm{ERF})} = (0, \xi, \eta)^\mathsf{T}$. In contrast, for $\bar{u}_A = (x, y, z)^\mathsf{T}$ as used below, $x \neq 0$ is possible. Accordingly, the evaluation of the triple cross product yields

$$
(44)\quad \bar{u}_A \times (\omega \times (\omega \times \bar{u}_A)) = \begin{pmatrix} \omega_y\omega_z \left(y^2 - z^2\right) + \left(\omega_z^2 - \omega_y^2\right) yz + \omega_x\omega_z xy - \omega_x\omega_y xz \\ \omega_x\omega_z \left(z^2 - x^2\right) + \left(\omega_x^2 - \omega_z^2\right) xz + \omega_x\omega_y yz - \omega_y\omega_z xy \\ \omega_x\omega_y \left(x^2 - y^2\right) + \left(\omega_y^2 - \omega_x^2\right) xy + \omega_y\omega_z xz - \omega_x\omega_z yz \end{pmatrix}.
$$

The FFR-transformed matrix of the second order cross-sectional moments in its general form is

$$
(45)\quad \begin{pmatrix} I_{xx} & I_{xy} & I_{xz} \\ I_{xy} & I_{yy} & I_{yz} \\ I_{xz} & I_{yz} & I_{zz} \end{pmatrix} = \int_A \rho \begin{pmatrix} y^2 + z^2 & -xy & -xz \\ -xy & x^2 + z^2 & -yz \\ -xz & -yz & x^2 + y^2 \end{pmatrix} \mathrm{d}A
$$

and can be obtained by rotating the ERF-oriented matrix of the second order cross-sectional moments:

$$
(46)\quad \begin{pmatrix} I_{xx} & I_{xy} & I_{xz} \\ I_{xy} & I_{yy} & I_{yz} \\ I_{xz} & I_{yz} & I_{zz} \end{pmatrix} = \mathbf{T}^\mathsf{T} \cdot \begin{pmatrix} I_{20} + I_{02} & 0 & 0 \\ 0 & I_{02} & -I_{11} \\ 0 & -I_{11} & I_{20} \end{pmatrix} \cdot \mathbf{T}
$$

The integrated and ρ-weighted triple cross product is then obtained as

$$
(47)\quad \int_A \rho \cdot \bar{u}_A \times (\omega \times (\omega \times \bar{u}_A))\, \mathrm{d}A = \begin{pmatrix} \omega_y\omega_z \left(I_{zz} - I_{yy}\right) - \left(\omega_z^2 - \omega_y^2\right) I_{yz} - \omega_x\omega_z I_{xy} + \omega_x\omega_y I_{xz} \\ \omega_x\omega_z \left(I_{xx} - I_{zz}\right) - \left(\omega_x^2 - \omega_z^2\right) I_{xz} - \omega_x\omega_y I_{yz} + \omega_y\omega_z I_{xy} \\ \omega_x\omega_y \left(I_{yy} - I_{xx}\right) - \left(\omega_y^2 - \omega_x^2\right) I_{xy} - \omega_y\omega_z I_{xz} + \omega_x\omega_z I_{yz} \end{pmatrix}.
$$

Finally, the centrifugal loads acting on flexible rotational motion are obtained:

$$(48)\quad Q^{f,c}_{v,\mathrm{rot}} = -\int_x \mathbf{S}^{\mathsf{T}}_{\mathrm{rot}} \left[\mathbf{T}^{\mathsf{T}} \cdot \begin{pmatrix} 0 \\ I_{10} \\ I_{01} \end{pmatrix} \times (a + \omega \times (\omega \times \bar{u}_m)) + \ldots \right.$$
$$\left. \ldots + \begin{pmatrix} \omega_y\omega_z\left(I_{zz} - I_{yy}\right) - \left(\omega_z^2 - \omega_y^2\right) I_{yz} - \omega_x\omega_z I_{xy} + \omega_x\omega_y I_{xz} \\ \omega_x\omega_z\left(I_{xx} - I_{zz}\right) - \left(\omega_x^2 - \omega_z^2\right) I_{xz} - \omega_x\omega_y I_{yz} + \omega_y\omega_z I_{xy} \\ \omega_x\omega_y\left(I_{yy} - I_{xx}\right) - \left(\omega_y^2 - \omega_x^2\right) I_{xy} - \omega_y\omega_z I_{xz} + \omega_x\omega_z I_{yz} \end{pmatrix} \right] \mathrm{d}x$$

For the effect of gyroscopic loads on the flexible rotational DoF, it is assumed that $\dot{\bar{u}} = \dot{\bar{u}}_{\mathrm{flex}} = \text{const.}$ over the section A, which is an acceptable simplification.

$$(49)\quad Q^{f,g}_{v,\mathrm{rot}} = -2\int_x \mathbf{S}^{\mathsf{T}}_{\mathrm{rot}} \int_A \rho \cdot \bar{u}_A \times (\omega \times \dot{\bar{u}})\, \mathrm{d}A\, \mathrm{d}x$$
$$= -2\int_x \mathbf{S}^{\mathsf{T}}_{\mathrm{rot}} \int_A \rho \cdot \bar{u}_A\, \mathrm{d}A \times (\omega \times \dot{\bar{u}})\, \mathrm{d}x$$
$$= -2\int_x \mathbf{S}^{\mathsf{T}}_{\mathrm{rot}} \left[\mathbf{T}^{\mathsf{T}} \cdot \begin{pmatrix} 0 \\ I_{10} \\ I_{01} \end{pmatrix} \times (\omega \times \dot{\bar{u}}) \right] \mathrm{d}x$$

A.3. Verification of the Propeller Moment

The configuration used to verify the propeller moment is illustrated in Figure A.1. The "beam" consists of 4 quasi-massless and torsionally soft FE elements (grey part of the beam), which together have the torsional stiffness k. The fifth and last element is a quasi-rigid cuboid of size $a \cdot a \cdot c$ with homogeneous mass density ρ (blue part of the beam). Note that the beam axis x is not kinked, i.e. the cuboid's longitudinal x-axis coincides with one of its shorter dimensions a and not with the longer side c. The beam is clamped to a hub rotating at constant speed Ω and has an undeformed inclination of θ_{pre}. Due to the propeller moment acting on the cuboid, the beam is elastically twisted by $\theta_{\mathrm{flex}} < 0$. The parameters of the beam configuration are listed in Table A.1.

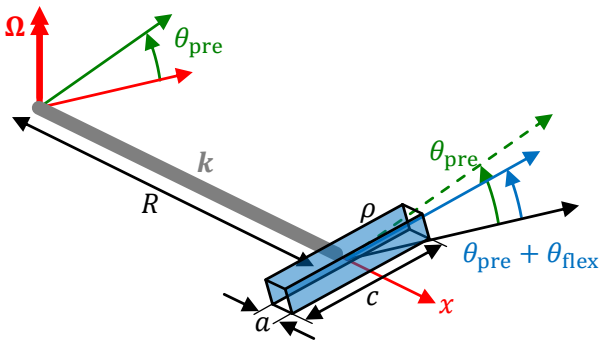

Figure A.1: Beam configuration for verifying the propeller moment

Table A.1: Parameters of the beam in Figure A.1

Ω	$100\,\mathrm{rad/s}$
θ_{pre}	$1\,^\circ$
k	$2750\,\mathrm{Nm/rad}$
R	$10\,\mathrm{m}$
a	$0.1\,\mathrm{m}$
c	$1.0\,\mathrm{m}$
ρ	$1000\,\mathrm{kg/m^3}$

The propeller moment acting on the cuboid with inclination $\theta = \theta_{\mathrm{pre}} + \theta_{\mathrm{flex}}$ is

$$(50)\quad M_p = -\Omega^2 \cdot \left(I_{zz} - I_{yy}\right) \cdot \sin(\theta) \cdot \cos(\theta),$$

where the mass moments of inertia are $I_{zz} = m/12\,\left(a^2 + c^2\right)$ and $I_{yy} = m/12\,\left(a^2 + a^2\right)$ with $m = \rho\, a^2\, c$. This term can, for example, be identified in the torsional differential equation in [11] and is explicitly called "propeller moment" in [9]. The torsional stiffness of the rotating beam in equilibrium counteracts the propeller moment, i.e. $\theta_{\mathrm{flex}} = M_p/k$. Since $\theta < 1\,^\circ$, the simplifications $\sin(\theta) \approx \theta$ and $\cos(\theta) \approx 1$ are justifiable so that

$$(51)\quad \theta_{\mathrm{flex}} = \frac{-\Omega^2}{k}\left(I_{zz} - I_{yy}\right) \cdot \left(\theta_{\mathrm{pre}} + \theta_{\mathrm{flex}}\right).$$

This yields

$$(52)\quad \theta_{\mathrm{flex}} = \frac{\frac{-\Omega^2}{k}\left(I_{zz} - I_{yy}\right)\theta_{\mathrm{pre}}}{1 + \frac{\Omega^2}{k}\left(I_{zz} - I_{yy}\right)} = -0.75^\circ.$$

In VAST, an equilibrium calculation is performed for this beam which is configured using BAM elements.

Table A.2 compares the resulting flexible tip twist for the three implementation variants described in Section 3 with the analytical solution. As expected,

Table A.2: Equilibrium flexible twist θ_{flex} of the beam in Figure A.1 with the parameters of Table A.1

Analytical	VAST baseline	VAST upgrade 1	VAST upgrade 2
$-0.75°$	$0°$	$-2.83°$	$-0.74°$

the baseline implementation does not account for the effect at all. Since upgrade 1 constantly applies the propeller moment at $\theta = \theta_{\text{pre}}$ regardless of θ_{flex}, the resulting θ_{flex} is strongly overpredicted in magnitude, which even results in a negative overall inclination $\theta < 0$ which is of course unphysical. Only when the dependence of inertial loads on deformation is respected (upgrade 2) is the result correct within the accuracy expected from the numerics and discretization.

To address the frequency-domain behavior of the beam, the restoring propeller moment can be interpreted as an additional stiffness (cf. Section 6), for which again the small angle assumption for θ is applied:

$$k_p = \partial M_p / \partial \theta = \Omega^2 \left(I_{zz} - I_{yy} \right) \tag{53}$$

The expected eigenfrequency of the torsional oscillation is

$$\omega = \sqrt{\frac{k + k_p}{I_{xx}}} \tag{54}$$

with $I_{xx} = m/12 \left(c^2 + a^2 \right)$. Table A.3 presents the eigenfrequencies of the first torsion mode T1 of the beam for the non-rotating case and for $\Omega = 100\,\text{rad/s}$. The analytical results are based on Equation 54, while the computational eigenfrequencies are obtained during modal reduction according to Section 6. In the non-rotating case, all results are identical which confirms consistency of the analytical and computational structural models (without inertial loads). At $\Omega = 100\,\text{rad/s}$, a T1 eigenfrequency of $18.19\,\text{Hz}$ is expected analytically. However, for both the baseline model and upgrade 1, only a slight increase in eigenfrequency compared to the non-rotating case is observed. The large part of the eigenfrequency increase is introduced by upgrade 2, since only this update models the spring-like behavior of the propeller moment, i.e. the additional stiffness according to Equation 53. The small increases in eigenfrequency from $\Omega = 0\,\text{rad/s}$ to $\Omega = 100\,\text{rad/s}$ observed from the baseline model and upgrade 1 are attributed to geometric stiffening effects, which are *not* considered in the analytical calculation. Also for upgrade 2 at $\Omega = 100\,\text{rad/s}$, such additional stiffening is observed since the simulated eigenfrequency of $18.33\,\text{Hz}$ is slightly higher than the analytical reference value.

Table A.3: T1 eigenfrequency of the beam in Figure A.1 with the parameters of Table A.1, also including the non-rotating case $\Omega = 0\,\text{rad/s}$

Ω	$0\,\text{rad/s}$	$100\,\text{rad/s}$
Analytical	$9.10\,\text{Hz}$	$18.19\,\text{Hz}$
VAST baseline	$9.10\,\text{Hz}$	$9.37\,\text{Hz}$
VAST upgrade 1	$9.10\,\text{Hz}$	$9.37\,\text{Hz}$
VAST upgrade 2	$9.10\,\text{Hz}$	$18.33\,\text{Hz}$

These comparisons of equilibrium flexible twist and torsion eigenfrequency demonstrate the distinct effects of upgrades 1 and 2 and successfully verify the implementation with upgrade 2 based on analytical reference results. The baseline method needs to be enhanced by both upgrades to obtain a model which accurately predicts the torsion dynamics of beams similar to rotor blades.

A.4. Verification of Inertial Loads with Accelerated FFR

The enhanced implementation of inertial loads Q_v^f according to Equation 11 and Equation 12 includes the translatory acceleration a of the FFR. It is verified based on the configuration shown in Figure A.2. The

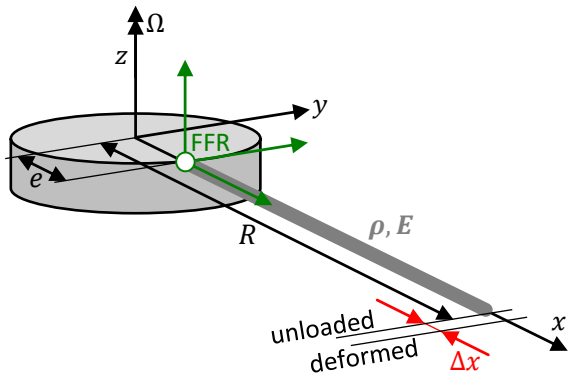

Figure A.2: Beam configuration to verify the effect of centrifugal loads for an accelerated FFR

aluminum beam (density ρ, Young's modulus E) is clamped to a rotating rigid hub (angular speed Ω) at radius e; the overall radius is R. The parameters are listed in Table A.4. The incremental centrifugal force in the beam at radius x (measured from the

Table A.4: Parameters of the beam in Figure A.2

Ω	$100\,\mathrm{rad/s}$
e	$1\,\mathrm{m}$
R	$3\,\mathrm{m}$
ρ	$2700\,\mathrm{kg/m^3}$
E	$70 \cdot 10^9\,\mathrm{N/m^2}$

rotor center) is

$$\mathrm{d}F_x(x) = \Omega^2 \cdot x \cdot \mathrm{d}m = \Omega^2 \cdot x \cdot \rho\, A\, \mathrm{d}x \tag{55}$$

where A is the beam's cross section area. Accordingly, the equilibrium tensile force in the beam is

$$\begin{aligned} F_x(x) &= \int_x^R \Omega^2 \cdot X \cdot \rho\, A\, \mathrm{d}X \\ &= \frac{\rho}{2} A\, \Omega^2 \left(R^2 - x^2\right). \end{aligned} \tag{56}$$

The axial strain distribution $\epsilon(x) = \sigma/E = F_x/(E\,A)$ is integrated over the flexible beam to calculate the tip displacement Δx:

$$\begin{aligned} \Delta x &= \int_e^R \epsilon(X)\, \mathrm{d}X \\ &= \frac{\rho}{2} \frac{1}{E\,A} A\, \Omega^2 \int_e^R R^2 - X^2\, \mathrm{d}X \\ &= \frac{\rho}{2} \frac{\Omega^2}{E} \left[R^2 X - \frac{X^3}{3}\right]_e^R \\ &= \frac{\rho}{2} \frac{\Omega^2}{E} \left[\frac{2}{3} R^3 + e\left(\frac{e^2}{3} - R^2\right)\right] \\ &\overset{\text{Table A.4}}{=} 1.8 \cdot 10^{-3}\,\mathrm{m} \end{aligned} \tag{57}$$

The same beam is configured in VAST-MBS using 20 equal BAM elements. The equilibrium is calculated numerically and the resulting tip displacement is compared to the analytical solution in Table A.5. Both the baseline and the corrected implementation are tested. As expected, the corrected variant yields the correct tip displacement, while the baseline implementation yields the displacement which would be obtained for $e = 0\,\mathrm{m}$ and $R = 2\,\mathrm{m}$, i.e. at the same rotor speed but without FFR acceleration a. Strictly speaking, this test only confirms the correctness of the inertial loads' effect on the translatory displacements, Equation 11. However, since the same centrifugal loads are involved in the effect on rotational displacements, Equation 12 is also considered verified.

A.5. Verification of External Loads Application

The application of external loads according to Section 5 is verified based on equilibrium calculations

Table A.5: Equilibrium tip displacement Δx of the beam in Figure A.2 with baseline and corrected term $Q^f_{v,\mathrm{tra}}$ compared to analytical results

Analytical (param.: Table A.4)	$1.8000 \cdot 10^{-3}\,\mathrm{m}$
VAST corrected, Equation 11	$1.7991 \cdot 10^{-3}\,\mathrm{m}$
VAST baseline, Equation 6	$1.0286 \cdot 10^{-3}\,\mathrm{m}$
Analytical ($e = 0\,\mathrm{m}$, $R = 2\,\mathrm{m}$)	$1.0286 \cdot 10^{-3}\,\mathrm{m}$

of a simple beam composed of 5 identical elements. The beam has a radius of $R = 10\,\mathrm{m}$, a quadratic cross-section of side length $a = 0.1\,\mathrm{m}$, Young's modulus $E = 210 \cdot 10^9\,\mathrm{N/m^2}$, and a Poisson's ratio of $\nu = 0.3$. The beam is loaded by discrete forces.

Figure A.3 shows a test case in which an eccentric force $F_z = 1000\,\mathrm{N}$ is applied at the beam tip with a lateral offset of $y(F_z) = 1\,\mathrm{m}$. The tip force causes a

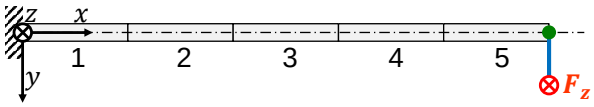

Figure A.3: Eccentric tip force

bending deformation of the beam axis, which would also occur for a centered applied force. Due to the small resulting tip twist angle of $\theta_{\mathrm{tip}} \approx 0.5\,^\circ$ (calculated further below), the simplification $\cos\left(\theta_{\mathrm{tip}}\right) \approx 1$ is justified. Accordingly, the calculation assumes an unchanged force F_z acting in the z-direction of the FFR. The bending in z-direction is described by

$$z''(x) = \frac{M_y(x)}{E\,I} = \frac{F_z \cdot (R - x)}{E\,I} \tag{58}$$

with $I = a^4/12 = 8.\bar{3} \cdot 10^{-6}\,\mathrm{m^4}$. Twofold integration under consideration of boundary conditions $z(0) = z'(0) = 0$ yields the cubic bending line

$$z(x) = \frac{F_z}{E\,I}\left(R \cdot \frac{x^2}{2} - \frac{x^3}{6}\right), \tag{59}$$

which evaluates to $z(R) = 0.19\,\mathrm{m}$ at the tip. The numerical results of the VAST equilibrium calculation are compared to the above calculated analytical results in Figure A.4. Therein, x is the undeformed radial coordinate.

On top of the bending deformation, due to eccentric application of F_z, a torsion moment $M_x = F_z \cdot y(F_z) = 1000\,\mathrm{Nm}$ arises which is constant along the radius x. This causes a linear twist distribution with tip deflection

$$\theta(R) = \frac{M_x \cdot R}{G\,J} = 0.0088\,\mathrm{rad} = 0.504^\circ \tag{60}$$

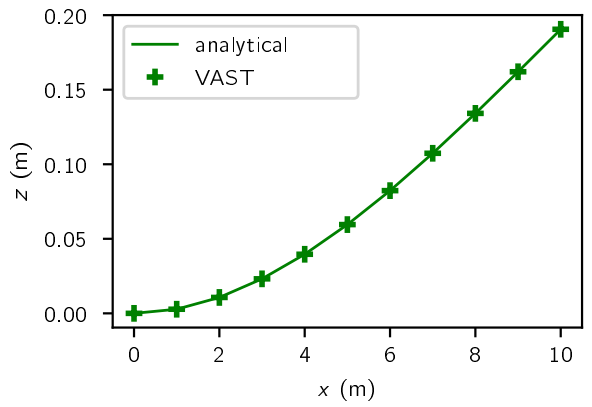

Figure A.4: Cubic bending line of beam in Figure A.3

where $G = 0.5\,E/(1+\nu)$ and $J = 2.25 \cdot (a/2)^4$ (torsion constant for quadratic cross sections[12]). The analytical twist distribution is shown in Figure A.5 along with the numerical results.

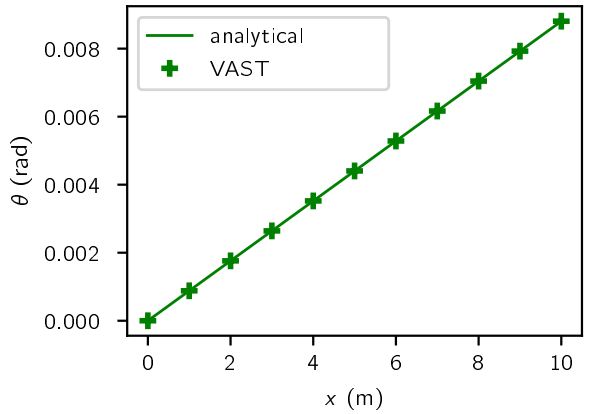

Figure A.5: Linear twist distribution of beam in Figure A.3

The numerical results of both bending line and twist distribution match perfectly with the analytical reference results. Consequently, this test case verifies the effect of eccentric forces on the beam deformation.

Figure A.6 depicts a test with two axial forces $F_x = 100 \cdot 10^3\,\mathrm{N}$; one acting at the tip and one acting at the middle of the beam, within element 3. Accordingly, the cross sections in the left half of the beam are loaded by $2\,F_x$, while those on the right half are loaded by F_x. The displacements in the middle and at the tip are calculated as follows, while the displacement distribution in between is linear.

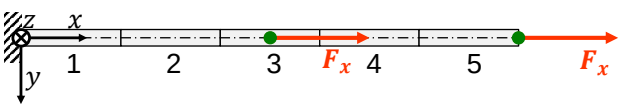

Figure A.6: Axial forces within an element and at the tip

$$\Delta x(R/2) = \frac{2\,F_x \cdot (R/2)}{E\,A} = 4.76 \cdot 10^{-4}\,\mathrm{m} \tag{61}$$

$$\begin{aligned}\Delta x(R) &= \Delta x(R/2) + \frac{F_x \cdot (R/2)}{E\,A} \\ &= 7.14 \cdot 10^{-4}\,\mathrm{m}\end{aligned} \tag{62}$$

The analytical and numerical results of elongation vs. undeformed radius are compared in Figure A.7. Although no node is located at a radius of $x = 5\,\mathrm{m}$ (this is the middle of element 3), the numerical result of the elongation correlates very well with the analytical prediction. In particular, the kink is well reproduced. Accordingly, this test case verifies the external force application within an element, i.e. between the nodes.

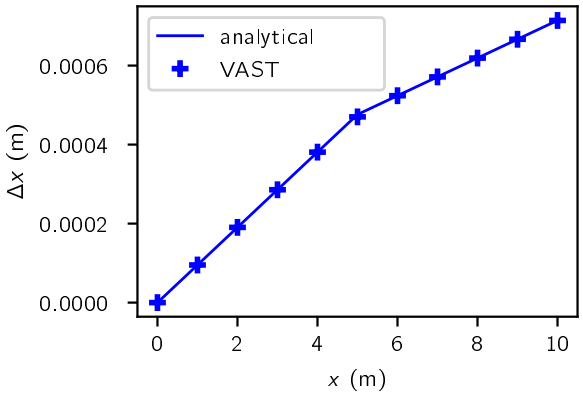

Figure A.7: Elongation distribution of beam in Figure A.6